



# A multiphase three-dimensional multi-relaxation time (MRT) lattice Boltzmann model with surface tension adjustment



Sami Ammar\*, Guillaume Pernaudat, Jean-Yves Trépanier

Department of Mechanical Engineering, École Polytechnique, 2500, chemin de Polytechnique, Montréal, H3T 1J4, Canada

## ARTICLE INFO

### Article history:

Received 24 February 2016

Received in revised form 10 February 2017

Accepted 16 April 2017

Available online 20 April 2017

### Keywords:

Multiphase flow

MRT lattice Boltzmann

Three-dimension

Adjustable surface tension

Large density ratios

## ABSTRACT

The interdependence of surface tension and density ratio is a weakness of pseudo-potential based lattice Boltzmann models (LB). In this paper, we propose a 3D multi-relaxation time (MRT) model for multiphase flows at large density ratios. The proposed model is capable of adjusting the surface tension independently of the density ratio. We also present the 3D macroscopic equations recovered by the proposed forcing scheme. A high order of isotropy for the interaction force is used to reduce the amplitude of spurious currents. The proposed 3D-MRT model is validated by verifying Laplace's law and by analyzing its thermodynamic consistency and the oscillation period of a deformed droplet. The model is then applied to the simulation of the impact of a droplet on a dry surface. Impact dynamics are determined and the maximum spread factor calculated for different Reynolds and Weber numbers. The numerical results are in agreement with data published in the literature. The influence of surface wettability on the spread factor is also investigated. Finally, our 3D-MRT model is applied to the simulation of the impact of a droplet on a wet surface. The propagation of transverse waves is observed on the liquid surface.

© 2017 Elsevier Inc. All rights reserved.

## 1. Introduction

Multiphase flows occur in a large spectrum of fluid flow problems. However, the numerical simulation of multiphase flows is relatively difficult because of the complexity of the physical phenomena involved. Traditionally, the resolution of multiphase flow has been performed using the Navier–Stokes equations coupled with Eulerian or Lagrangian methods to define the position of the interface between the phases. The most common methods to capture the interfaces are: the Volume of Fluid method [1–3] and the Level Set method [4,5]. These methods capture the interface between two phases through a variable number of cells. For the Lagrangian method, the interface between different phases of the flow is explicitly obtained and can be tracked during the solution.

In recent decades, the lattice Boltzmann method (LBM) has emerged as an alternative to simulating multiphase flows [6]. This numerical method is an extension of cellular automata and uses distribution functions. LBM is now a popular alternative to conventional Computational Fluid Dynamics (CFD) methods to solve fluid flow problems with complex physics. The linearity of the propagation operators makes its implementation straightforward [7]. In the particular case of multiphase flows, it avoids reconstruction or tracking of the interface since the interface between phases appears automatically during the solution process. The interface is characterized by the variation of fluid densities and has a width of a few lattice nodes.

\* Corresponding author.

E-mail address: drsami.ammar@gmail.com (S. Ammar).

Several variants of multiphase flow models based on the lattice Boltzmann method have been developed. The first, known as Rothman and Keller [8], uses a color gradient to separate and model the interface between phases. The second is the pseudo-potential model [9] which uses a non-local interaction between particles to simulate the spontaneous segregation of the phase. The third variant is the free energy model proposed by Swift et al. [10,11] for which specialized collision rules are applied to ensure that the system converges to the minimum of the free energy functional [7].

Because of its simplicity and versatility, the pseudo-potential model proposed by Shan and Chen [9,12] is one of the most popular multiphase lattice Boltzmann models. The general idea behind this model is to use a pseudo-potential that depends on the local fluid density to represent the microscopic interactions at the mesoscopic scale. Thus, if the intensity of interaction  $g$  (function of temperature) is below a critical value ( $g < g_c$ ), automatic phase separation occurs, resulting in a low-density phase and a high density phase. In the opposite case, when the value of the intensity of interaction is greater than the critical value, the coexistence of both liquid and gas is not possible [13]. This automatic segregation is an important feature of the pseudo-potential model and makes it very attractive to many users. In view of its effectiveness and its ability to represent the underlying microscopic physics, this approach has been chosen in the present work.

However, the original pseudo-potential model has some limitations. First, it suffers from a density ratio limit between phases. Increasing the density ratio involves an increase in spurious currents which increases the risk of numerical instabilities. To overcome this limitation, in recent decades several modifications have been proposed in the literature: the isothermal equation of state can be replaced by a realistic equation of state (EOS) [14,15]; the isotropic order of the gradient operator can be increased [16,17]; or, finally, the width of the interface can be increased [16]. A second limitation is the dependency between the surface tension and the density ratio [16]. For example, when introducing a realistic equation of state as in Yuan and Schaefer's method [15], both the density ratio and surface tension vary with the temperature since temperature is the only free parameter. In order to tune the surface tension independently of the density ratio, Sbragaglia et al. [16] developed a multi-range potential where he proposes to add a second force term into the interaction force. There are now two tunable parameters and, therefore, the surface tension and density ratio can be controlled separately. However, in a recent study, Huang et al. [18] reported that the density ratio is considerably modified when the multi-range potential is used to adjust the surface tension. Li et al. [19] explain the reasoning through theoretical and numerical analyzes of the multi-range potential: the mechanical stability condition varies according to two parameters of the multi-range potential which results in a violation of the thermodynamic consistency. To adjust the surface tension independently, Li et al. [19] then proposed an alternative approach which consisted of modifying the pressure tensor of the pseudo-potential model based on the 2D multiple relaxation time (MRT) model. Compared to Sbragaglia's model [16], this model gave a density distribution independent of other properties and allowed the surface tension to change over a wide range of values. Later, Xu et al. [20] modified the pressure tensor of the original pseudo-potential model based on a lattice D3Q15.

In parallel, to improve the stability of the pseudo-potential model, Kupershtokh et al. [14,21,22] showed that the calculation of the interaction force plays an important role in preserving the thermodynamic consistency. They reduced the thermodynamic inconsistency of the Van der Waals EOS by combining the local approximation and the mean-value approximation for the calculation of the interaction force. They also found that this interaction force allowed extension of the stable temperature range and reduced spurious currents [13]. Finally, in order to adjust the surface tension, Hu et al. [23] proposed modifying the pressure tensor of Kupershtokh's model in a 2D-MRT operator.

Since multiphase problems are three-dimensional by nature, in the present work we set out to develop a 3D-MRT model in which the surface tension could be adjusted by modifying the pressure tensor. Our new model is an extension of Hu's model to a 3D-MRT model based on the D3Q19 lattice. There are major differences in the development of a 2D-MRT model and a 3D-MRT model, which are discussed in Section 2. We present the theoretical development of our 3D-MRT model by detailing the force term and source term. We also give the macroscopic equations of multiphase flow for the 3D case. The Chapman Enskog analysis was used to provide the relationship between the moment bases and force terms including the surface tension force. To limit spurious currents, we apply a high isotropy order of the interaction force into the 3D-MRT model and perform an analysis of the spurious currents versus the isotropic order. The new pseudo-potential model is capable of simulating 3D problems at large density ratios with adjustable surface tension while maintaining the thermodynamic consistency and limiting spurious currents. Finally, we apply the proposed 3D-MRT model in the case of the droplet impact on a dry and wet surface.

The rest of the paper is organized as follows. Section 2 describes our numerical 3D-MRT multiphase model. The methods applied in order to increase the ratio density, decrease the spurious currents, ensure thermodynamic consistency and adjust the surface tension are presented in this section. In Section 3, applications for 3D-MRT model are presented and the results compared to literature. Finally, Section 4 presents our conclusions.

## 2. Numerical model

### 2.1. 3D single and multiple relaxation-time LBM model

The lattice Boltzmann method is a mesoscopic method for solving fluid flow. It uses distribution functions to calculate macroscopic quantities such as density, momentum and energy. Using the Guo force scheme [24], the lattice Boltzmann equation can be written as follows:

$$f_\alpha(\mathbf{x} + \mathbf{e}_\alpha \Delta t, t + \Delta t) - f_\alpha(\mathbf{x}, t) = \Omega_\alpha + \delta_t F_\alpha. \quad (1)$$

Where is the distribution function along the  $\alpha$ th direction at a node  $\mathbf{x}$  and time  $t$ ,  $\vec{e}_\alpha$  is the discrete velocity in the  $\alpha$ th direction,  $\delta_t$  is the time step,  $F_\alpha$  represents the forcing term and  $\Omega_\alpha$  is the collision operator.

For the single relaxation-time collision operator of Bhatnagar–Gross–Krook (BGK) type [25], the collision operator  $\Omega_\alpha$  is defined as:

$$\Omega_\alpha = -\frac{\delta_t}{\tau} (f_\alpha(\mathbf{x}, t) - f_\alpha^{eq}(\mathbf{x}, t)) \quad (2)$$

where  $f_\alpha^{eq}(\vec{x}, t)$  is the equilibrium distribution function and  $\tau$  the relaxation time. The equilibrium distribution function  $f_\alpha^{eq}(\vec{x}, t)$  can be written as follows:

$$f_\alpha^{eq} = \rho w_\alpha \left[ 1 + \frac{\mathbf{e}_\alpha \cdot \mathbf{u}}{c_s^2} + \frac{(\mathbf{e}_\alpha \cdot \mathbf{u})^2}{2c_s^4} - \frac{\mathbf{u} \cdot \mathbf{u}}{2c_s^2} \right] \quad (3)$$

where  $w_\alpha$  is the weighting factor. In the present study, the D3Q19 lattice is used for the 3D simulations. The discrete velocity and the weighting factor for the D3Q19 lattice are given by:

$$\begin{aligned} & [\mathbf{e}_0, \mathbf{e}_1, \mathbf{e}_2, \mathbf{e}_3, \mathbf{e}_4, \mathbf{e}_5, \mathbf{e}_6, \mathbf{e}_7, \mathbf{e}_8, \mathbf{e}_9, \mathbf{e}_{10}, \mathbf{e}_{11}, \mathbf{e}_{12}, \mathbf{e}_{13}, \mathbf{e}_{14}, \mathbf{e}_{15}, \mathbf{e}_{16}, \mathbf{e}_{17}, \mathbf{e}_{18}] \\ &= \begin{bmatrix} 0 & 1 & -1 & 0 & 0 & 0 & 0 & 1 & 1 & -1 & -1 & 1 & -1 & 1 & -1 & 0 & 0 & 0 & 0 \\ 0 & 0 & 0 & 1 & -1 & 0 & 0 & 1 & -1 & 1 & -1 & 0 & 0 & 0 & 0 & 1 & 1 & -1 & -1 \\ 0 & 0 & 0 & 0 & 0 & 1 & -1 & 0 & 0 & 0 & 0 & 1 & 1 & -1 & -1 & 1 & -1 & 1 & -1 \end{bmatrix} \end{aligned} \quad (4)$$

and

$$w_\alpha = \begin{cases} 1/3, & \alpha = 0; \\ 1/18, & \alpha = 1, 2, \dots, 6; \\ 1/36, & \alpha = 7, 8, \dots, 18. \end{cases} \quad (5)$$

the collision operator BGK uses a single relaxation time for all physical quantities. In order to improve relaxation, D'Humières [26] developed a model based on multiple relaxation times, where each physical quantity has its own characteristic time. The impact of using the MRT operator is an improved numerical stability. The MRT collision operator  $\Omega_\alpha$  is defined as [27]:

$$\Omega_\alpha = -(\mathbf{M}^{-1} \mathbf{\Lambda} \mathbf{M})_{\alpha\beta} (f_\alpha(\mathbf{x}, t) - f_\alpha^{eq}(\mathbf{x}, t)) \quad (6)$$

where  $\mathbf{M}^{-1} \mathbf{\Lambda} \mathbf{M}$  is the collision matrix. For the D3Q19 lattice, the transformation matrix  $\mathbf{M}$  is given by [26]:

$$\mathbf{M} = \begin{pmatrix} 1 & 1 & 1 & 1 & 1 & 1 & 1 & 1 & 1 & 1 & 1 & 1 & 1 & 1 & 1 & 1 & 1 & 1 & 1 \\ -30 & -11 & -11 & -11 & -11 & -11 & -11 & 8 & 8 & 8 & 8 & 8 & 8 & 8 & 8 & 8 & 8 & 8 & 8 \\ 12 & -4 & -4 & -4 & -4 & -4 & -4 & 1 & 1 & 1 & 1 & 1 & 1 & 1 & 1 & 1 & 1 & 1 & 1 \\ 0 & 1 & 0 & 0 & -1 & 0 & 0 & 1 & 1 & 0 & -1 & -1 & 0 & 1 & 1 & 0 & -1 & -1 & 0 \\ 0 & -4 & 0 & 0 & 4 & 0 & 0 & 1 & 1 & 0 & -1 & -1 & 0 & 1 & 1 & 0 & -1 & -1 & 0 \\ 0 & 0 & 1 & 0 & 0 & -1 & 0 & 1 & 0 & 1 & -1 & 0 & -1 & -1 & 0 & 1 & 1 & 0 & -1 \\ 0 & 0 & -4 & 0 & 0 & 4 & 0 & 1 & 0 & 1 & -1 & 0 & -1 & -1 & 0 & 1 & 1 & 0 & -1 \\ 0 & 0 & 0 & 1 & 0 & 0 & -1 & 0 & 1 & 1 & 0 & -1 & -1 & 0 & -1 & 0 & 1 & 0 & 1 \\ 0 & 0 & 0 & -4 & 0 & 0 & 4 & 0 & 1 & 1 & 0 & -1 & -1 & 0 & -1 & -1 & 0 & 1 & 1 \\ 0 & 2 & -1 & -1 & 2 & -1 & -1 & 1 & 1 & -2 & 1 & 1 & -2 & 1 & 1 & -2 & 1 & 1 & -2 \\ 0 & -4 & 2 & 2 & -4 & 2 & 2 & 1 & 1 & -2 & 1 & 1 & -2 & 1 & 1 & -2 & 1 & 1 & -2 \\ 0 & 0 & 1 & -1 & 0 & 1 & -1 & 1 & -1 & 0 & 1 & -1 & 0 & 1 & -1 & 0 & 1 & -1 & 0 \\ 0 & 0 & -2 & 2 & 0 & -2 & 2 & 1 & -1 & 0 & 1 & -1 & 0 & 1 & -1 & 0 & 1 & -1 & 0 \\ 0 & 0 & 0 & 0 & 0 & 0 & 0 & 1 & 0 & 0 & 1 & 0 & 0 & -1 & 0 & 0 & -1 & 0 & 0 \\ 0 & 0 & 0 & 0 & 0 & 0 & 0 & 0 & 0 & 1 & 0 & 0 & 1 & 0 & 0 & -1 & 0 & 0 & -1 \\ 0 & 0 & 0 & 0 & 0 & 0 & 0 & 0 & 0 & 1 & 0 & 0 & 1 & 0 & 0 & -1 & 0 & 0 & -1 \\ 0 & 0 & 0 & 0 & 0 & 0 & 0 & 0 & 1 & -1 & 0 & -1 & 1 & 0 & 1 & -1 & 0 & -1 & 1 \\ 0 & 0 & 0 & 0 & 0 & 0 & 0 & -1 & 0 & 1 & 1 & 0 & -1 & 1 & 0 & 1 & -1 & 0 & -1 \\ 0 & 0 & 0 & 0 & 0 & 0 & 0 & 0 & 1 & -1 & 0 & -1 & 1 & 0 & -1 & 1 & 0 & 1 & -1 \end{pmatrix} \quad (7)$$

And the diagonal matrix  $\mathbf{\Lambda}$  of relaxation parameters is given by:

$$\mathbf{\Lambda} = \text{diag}(s_1, s_2, s_3, s_4, s_5, s_6, s_7, s_8, s_9, s_{10}, s_{11}, s_{12}, s_{13}, s_{14}, s_{15}, s_{16}, s_{17}, s_{18}, s_{19}) \quad (8)$$

$s_1, s_4, s_6$  and  $s_8$  correspond to the relaxation parameters associated with invariants  $\rho, j_x, j_y, j_z$  respectively and therefore, the value of these parameters does not matter. The relaxation parameter  $s_2$  is related to the bulk viscosity and the relaxation parameters  $s_{10}, s_{12}, s_{14}, s_{15}$  and  $s_{16}$  are related to the viscosity.  $s_{11}, s_{13}, s_{17}, s_{18}$  and  $s_{19}$  are free parameters.

Unlike the BGK collision operator, the MRT collision operator is calculated in the moment space. The distribution function  $f$  and the equilibrium distribution function  $f^{eq}$  are transferred in moments space after multiplication by the transformation matrix  $\mathbf{M}$  as follows:  $m = \mathbf{M}f$  and  $m^{eq} = \mathbf{M}f^{eq}$ . Therefore, the lattice Boltzmann equation (Eq. (1)) in the moment space can be written as:

$$\mathbf{m}^* = \mathbf{m} - \mathbf{S}(\mathbf{m} - \mathbf{m}^{eq}) + \left( \mathbf{I} - \frac{\mathbf{\Lambda}}{2} \right) \mathbf{S} \quad (9)$$

where  $I$  is the unit tensor, and the equilibrium moments  $\mathbf{m}^{eq}$  are given by:

$$\mathbf{m}^{eq} = \begin{bmatrix} r \\ -11r + 19 \frac{j_x^2 + j_y^2 + j_z^2}{r} \\ 3r - \frac{11}{2} \frac{j_x^2 + j_y^2 + j_z^2}{r} \\ j_x \\ -\frac{2}{3} j_x \\ j_y \\ -\frac{2}{3} j_y \\ j_z \\ -\frac{2}{3} j_z \\ \frac{2j_x^2 - (j_y^2 + j_z^2)}{r} \\ -\frac{1}{2} \frac{2j_x^2 - (j_y^2 + j_z^2)}{r} \\ \frac{j_y^2 - j_z^2}{r} \\ \frac{j_x j_y}{r} \\ \frac{j_y j_z}{r} \\ \frac{j_x j_z}{r} \\ 0 \\ 0 \\ 0 \end{bmatrix} \quad (10)$$

where  $j_x = \rho u_x$ ,  $j_y = \rho u_y$ ,  $j_z = \rho u_z$  are the momentum of  $x$ ,  $y$ , and  $z$  directions respectively.

The force term in the moment space is given by:

$$\mathbf{M}\mathbf{F}' = \left( \mathbf{I} - \frac{\Lambda}{2} \right) \mathbf{S} \quad (11)$$

where  $\mathbf{S}$  is given by:

$$\mathbf{S} = \begin{bmatrix} 0 \\ 38(u_x F_x + u_y F_y + u_z F_z) \\ -11(u_x F_x + u_y F_y + u_z F_z) \\ F_x \\ -\frac{2}{3} F_x \\ F_y \\ -\frac{2}{3} F_y \\ F_z \\ -\frac{2}{3} F_z \\ 2(2u_x F_x - u_y F_y - u_z F_z) \\ -2u_x F_x + u_y F_y + u_z F_z \\ 2(u_y F_y - u_z F_z) \\ -u_y F_y + u_z F_z \\ u_y F_x + u_x F_y \\ u_z F_y + u_y F_z \\ u_z F_x + u_x F_z \\ 0 \\ 0 \\ 0 \end{bmatrix} \quad (12)$$

with  $F^2 = F_x^2 + F_y^2 + F_z^2$ .

The bulk viscosity  $\xi$  and the kinematic viscosity in the MRT model are given by:

$$\xi = \frac{2}{9} \left( \frac{1}{s_2} - \frac{1}{2} \right) \quad (13)$$

and

$$\nu = \frac{1}{3} \left( \frac{1}{s_\beta} - \frac{1}{2} \right), \quad \beta = 10, 12, 14, 15, 16 \quad (14)$$

Finally, the macroscopic density and velocity are calculated by:

$$\rho(\mathbf{x}, t) = \sum_{\alpha=1}^N f_{\alpha}(\mathbf{x}, t) \quad (15)$$

$$\rho \mathbf{u}(\mathbf{x}, t) = \sum_{\alpha=1}^N \mathbf{e}_{\alpha} f_{\alpha}(\mathbf{x}, t) + \frac{\mathbf{F}}{2} \quad (16)$$

## 2.2. The pseudo-potential model

We base our 3D-MRT multiphase model on the pseudo-potential model. For the present work, Kupershtokh's model [14] is selected. Compared to the original pseudo-potential model, this one reduce spurious currents and thermodynamic inconsistency [14]. The interaction force of Kupershtokh's model is given by:

$$\mathbf{F}(\mathbf{x}) = -A \frac{G}{2} \psi(\mathbf{x}) c_s^2 \sum_{\alpha=1}^{18} w(|\mathbf{e}_{\alpha}|^2) U(\mathbf{x} + \mathbf{e}_{\alpha}) \mathbf{e}_{\alpha} - \frac{1-A}{2} G \psi(\mathbf{x}) c_s^2 \sum_{\alpha=1}^{18} w(|\mathbf{e}_{\alpha}|^2) \psi(\mathbf{x} + \mathbf{e}_{\alpha}) \mathbf{e}_{\alpha} \quad (17)$$

where  $\psi$  is the interaction potential (also called effective mass) that depends on the local fluid density.  $U(\mathbf{x}, t)$  is the potential function equal to  $G\psi(\mathbf{x}, t)^2/2$ , and  $A$  is a parameter which can be adjusted to reduce the thermodynamic inconsistency. The mechanical stability condition is given as  $\mathbf{e} = -2\alpha/\beta$ . The values of  $\alpha$  and  $\beta$  depend on parameter  $A$  and are given by  $\alpha = 3A$  and  $\beta = 3$  [23].

## 2.3. Equations of state

Various equations of state (EOS) including: the Van der Waals (VdW) EOS, the Redlich Kwong (R-K) EOS, the Peng–Robinson (P-R) EOS and the Carnahan–Starling (C-S) EOS, were analyzed in Yuan and Schaefer's study [15]. They showed that the C-S EOS enabled the maximum density ratio over a wide stable temperature range while minimizing the spurious currents around the interface. In fact, high density ratios in the order  $O(1000)$  were reached. Thus, C-S EOS is used in the present multiphase model. The C-S EOS is given by:

$$p = \rho RT \frac{1 + b\rho/4 + (b\rho/4)^2 - (b\rho/4)^3}{(1 - b\rho/4)^3} - a\rho \quad (18)$$

where  $a = 0.4963(RT_c)^2/p_c$ ,  $b = 0.1873RT_c/p_c$ .  $T_c$  and  $p_c$  are respectively the critical temperature and critical pressure. In the present study, the parameters are fixed  $a = 1$ ,  $b = 4$ ,  $R = 1$  [15]. The corresponding critical temperature and pressure values were, respectively,  $T_c = 0.094325$  and  $p_c = 0.0044$ .

The interaction potential is defined as a function of the pressure, as follows:

$$\psi = \sqrt{\frac{2}{Gc_s^2}(p - \rho c_s^2)} \quad (19)$$

Substituting Eq. (18) into Eq. (19), the effective mass becomes:

$$\psi = \sqrt{\frac{2}{Gc_s^2} \left( \rho RT \frac{1 + b\rho/4 + (b\rho/4)^2 - (b\rho/4)^3}{(1 - b\rho/4)^3} - a\rho - \rho c_s^2 \right)} \quad (20)$$

## 2.4. Higher order isotropy

Sbragaglia et al. [16] has shown that spurious currents result from a lack of isotropy in the interaction force [16]. He proposed reducing the spurious currents by increasing the isotropic order. The extended interaction potential method proposed by Sbragaglia et al. is implemented in the present work.

To achieve a higher isotropy order, the interaction force requires a larger number of neighboring nodes. Applying a Taylor expansion to  $\psi(\bar{\mathbf{x}} + \vec{e}_{\alpha})$ , the interaction force is rewritten as follows [16]:

$$\mathbf{F}_f = -G\psi(\mathbf{x})c_s^2 \sum_{n=0}^{\infty} \frac{1}{n!} E^{(n+1)} \nabla^n \psi(\mathbf{x}) \quad (21)$$

**Table 1**  
Weights for isotropy order of 6, 8, 10 in 3D case [16].

Tensor	w(1)	w(2)	w(3)	w(4)	w(5)	w(6)	w(8)	w <sub>221</sub> (9)	w <sub>300</sub> (9)	w(10)	w(11)
$E^{(6)}$	$\frac{2}{15}$	$\frac{1}{15}$	$\frac{1}{60}$	$\frac{1}{120}$							
$E^{(8)}$	$\frac{4}{45}$	$\frac{1}{21}$	$\frac{2}{105}$	$\frac{1}{104}$	$\frac{1}{315}$	$\frac{1}{630}$	$\frac{1}{5040}$				
$E^{(10)}$	$\frac{352}{5355}$	$\frac{38}{1071}$	$\frac{271}{14280}$	$\frac{139}{14280}$	$\frac{53}{10710}$	$\frac{5}{2142}$	$\frac{41}{85680}$	$\frac{1}{4284}$	$\frac{1}{5355}$	$\frac{1}{10710}$	$\frac{1}{42840}$

With:

$$E^{(n)} = E_{i_1 \dots i_n}^{(n)} = \sum_{n=0}^N w(|e_\alpha|^2) e_\alpha^{i_1} e_\alpha^{i_2} \dots e_\alpha^{i_n} \quad (22)$$

where  $N$  is the neighboring nodes number used. The odd tensor  $E^{(2n+1)}$  was zero. Table 1 gives the weights  $w(|e_\alpha|^2)$  as a function of the isotropic order in the 3D case. In the present study, all simulations, except those in section 3.1, are performed with an isotropic order of 8.

We note that the weights for velocities  $|e_\alpha|^2 = 9$  must be chosen based on the  $x, y, z$  directions in space [16].

### 2.5. Adjustment of the surface tension

To our knowledge, no 3D multiphase model allows a change in surface tension without a change in the density distribution, which affects thermodynamic consistency. In the present work, we propose an extension of the 2D-MRT model of Hu et al. [23] to a 3D-MRT model based on the D3Q19 lattice in order to decouple the surface tension and the density distribution while respecting thermodynamic consistency.

Following Li et al. [19], we modify the pressure tensor by adding a source term  $C$  to the MRT-lattice Boltzmann equation (Eq. (9)) as follows:

$$m^* = m - S(m - m^{eq}) + \delta_t \left( I - \frac{\Lambda}{2} \right) S + C \quad (23)$$

This new approach allows us to adjust the surface tension independently and avoid affecting the mechanical stability condition and thus modifying the density distribution. The thermodynamic consistency is respected by adjusting the parameter  $A$  in the source  $C$  term (Eq. (17)).

Based on the study of Hu et al. [23], we derive a generalization of the three-dimensional macroscopic equations which satisfy pressure tensor modification:

$$\partial_t \rho + \partial_x(\rho u_x) + \partial_y(\rho u_y) + \partial_z(\rho u_z) = 0 \quad (24)$$

$$\begin{aligned} & \partial_t(\rho u_x) + \partial_x(\rho u_x u_x) + \partial_y(\rho u_x u_y) + \partial_z(\rho u_x u_z) \\ &= -\partial_x(\rho c_s^2) + F_x + \partial_x \left[ 2v \left( \partial_x(\rho u_x) - \frac{1}{3} \nabla \cdot (\rho \mathbf{u}) \right) + \xi \nabla \cdot (\rho \mathbf{u}) \right] + \partial_y(v(\partial_x(\rho u_x) + \partial_y(\rho u_x))) \\ & \quad + \partial_z(v(\partial_x(\rho u_z) + \partial_z(\rho u_x))) + \partial_x \left[ \kappa \left( \left( \frac{Gc^4}{6} (\psi \nabla^2 \psi + A(\nabla \psi)^2) \right) \mathbf{I} - \frac{Gc^4}{6} (\psi \nabla \nabla \psi + A(\nabla \psi)^2) \right) \right] \end{aligned} \quad (25)$$

$$\begin{aligned} & \partial_t(\rho u_y) + \partial_x(\rho u_y u_x) + \partial_y(\rho u_y u_y) + \partial_z(\rho u_y u_z) \\ &= -\partial_y(\rho c_s^2) + F_y + \partial_x(v(\partial_x(\rho u_y) + \partial_y(\rho u_y))) + \partial_y \left[ 2v \left( \partial_y(\rho u_y) - \frac{1}{3} \nabla \cdot (\rho \mathbf{u}) \right) + \xi \nabla \cdot (\rho \mathbf{u}) \right] \\ & \quad + \partial_z(v(\partial_x(\rho u_z) + \partial_z(\rho u_x))) + \partial_y \left[ \kappa \left( \left( \frac{Gc^4}{6} (\psi \nabla^2 \psi + A(\nabla \psi)^2) \right) \mathbf{I} - \frac{Gc^4}{6} (\psi \nabla \nabla \psi + A(\nabla \psi)^2) \right) \right] \\ & \quad + O(\partial^5) \end{aligned} \quad (26)$$

$$\begin{aligned} & \partial_t(\rho u_z) + \partial_x(\rho u_z u_x) + \partial_y(\rho u_z u_y) + \partial_z(\rho u_z u_z) \\ &= -\partial_z(\rho c_s^2) + F_z + \partial_x(v(\partial_x(\rho u_z) + \partial_z(\rho u_x))) + \partial_z(v(\partial_x(\rho u_z) + \partial_z(\rho u_x))) \\ & \quad + \partial_z \left[ 2v \left( \partial_z(\rho u_z) - \frac{1}{3} \nabla \cdot (\rho \mathbf{u}) \right) + \xi \nabla \cdot (\rho \mathbf{u}) \right] \\ & \quad - \partial_z \left[ \kappa \left( \left( \frac{Gc^4}{6} (\psi \nabla^2 \psi + A(\nabla \psi)^2) \right) \mathbf{I} - \frac{Gc^4}{6} (\psi \nabla \nabla \psi + A(\nabla \psi)^2) \right) \right] + O(\partial^5) \end{aligned} \quad (27)$$

The parameter  $\kappa$ , varying from 0 to 1, is used to adjust the surface tension. According to Eqs. (25)–(27), the new pressure tensor is defined as:

$$\nabla \cdot \mathbf{P}_{new} = \nabla \cdot \mathbf{P} - \kappa \left( \left( \frac{Gc^4}{6} (\psi \nabla^2 \psi + A(\nabla \psi)^2) \right) \mathbf{I} - \frac{Gc^4}{6} (\psi \nabla \nabla \psi + A(\nabla \psi)^2) \right)$$

where

$$\nabla \cdot \mathbf{P} = \nabla \cdot (\rho c_s^2 \mathbf{I}) - \mathbf{F}$$

when  $\kappa$  is set to 0, we retrieve the pressure tensor of the pseudo-potential model without surface tension adjustment. In the present model, the new tensor pressure introduces the term  $\frac{Gc^4}{6}(1 - \kappa)(\psi \nabla \nabla \psi + A(\nabla \psi)^2)$  which determines the surface tension. Thus, when  $\kappa$  increases over the value range from 0 to 1, the surface tension decreases to approach zero.

According to the Chapman–Enskog analysis [28], the 3D-MRT source term  $\mathbf{C}$  is given by:

$$\mathbf{C} = \begin{bmatrix} 0 \\ \frac{2}{5}s_v(Q_{xx} + Q_{yy} + Q_{zz}) \\ 0 \\ 0 \\ 0 \\ 0 \\ 0 \\ 0 \\ 0 \\ -s_v(2Q_{xx} - Q_{yy} - Q_{zz}) \\ 0 \\ -s_v(Q_{yy} - Q_{zz}) \\ 0 \\ -s_v Q_{xy} \\ -s_v Q_{yz} \\ -s_v Q_{xz} \\ 0 \\ 0 \\ 0 \end{bmatrix} \quad (28)$$

The terms  $Q_{xx}$ ,  $Q_{yy}$ ,  $Q_{zz}$ ,  $Q_{xy}$ ,  $Q_{xz}$  and  $Q_{yz}$  are calculated from the following equation [23]:

$$\mathbf{Q} = \kappa \left[ (1 - A)\psi(\mathbf{x}) \sum_{\alpha=1}^{18} w(|\mathbf{e}_\alpha|^2) [\psi(\mathbf{x} + \mathbf{e}_\alpha) - \psi(\mathbf{x})] + \frac{1}{2} A \sum_{\alpha=1}^{18} w(|\mathbf{e}_\alpha|^2) [\psi(\mathbf{x} + \mathbf{e}_\alpha)^2 - \psi(\mathbf{x})^2] \right] \quad (29)$$

## 2.6. Total force

The total force  $\mathbf{F}$  acting on a fluid particle is the sum of all forces: the fluid–fluid interaction force  $F_f$  (Eq. (17)), the fluid–solid interaction force  $F_w$  (Eq. (30)) and the gravity force  $F_g$  (Eq. (31)).

When a fluid is in contact with a wall, the fluid–solid interaction force is calculated as follows [29]:

$$\mathbf{F}_w(\mathbf{x}) = -G_w \psi(\mathbf{e}_\alpha) \sum_{\alpha=1}^{18} w(|\mathbf{e}_\alpha|^2) \psi(\rho_w) s(\mathbf{x} + \mathbf{e}_\alpha) \mathbf{e}_\alpha \quad (30)$$

where  $s$  is a parameter, which is equal to 1 for a solid node and 0 for a fluid node. Here, we set the parameter  $G_w$  to  $-1$  and  $\rho_w$  is varied to achieve different contact angles and surface wettability. The surface wettability is the subject of some research studies [30–33]. The contact angle between a fluid and a solid wall is a measure of wetting surface (hydrophilic) or non-wetting surface (hydrophobic). If the angle contact is less than  $90^\circ$ , the droplet has a tendency to spread easily over the surface, which is referred to as a hydrophilic surface. Otherwise, if the contact angle is greater than  $90^\circ$ , the contact surface of the droplet over the surface is minimal, referred to, in this case, as a hydrophobic surface.

Finally, the gravity force is implemented as follows:

$$\mathbf{F}_g = \rho \mathbf{g} \quad (31)$$

## 3. Applications and results

In this section, we present the results of applying the 3D-MRT model as developed in various test cases. The model is evaluated by an analysis of spurious currents, by validation of Laplace’s law, verification of the thermodynamic consistency and an analysis of the oscillation dynamics of a deformed droplet. Finally, 3D applications of the model are made. The simulation and analysis of a liquid droplet impacting on dry and wet surfaces are performed. In all simulations, the parameter  $A$  in Eq. (17) is set at  $A = -0.55$  and the parameter  $\kappa$  in Eq. (29) is set as,  $\kappa = 0$ , except in section 3.2.

**Table 2**  
Maximum amplitude of the spurious velocity  $|u|_{max}$  for different isotropic order.

	4th order isotropy	6th order isotropy	8th order isotropy	10th order isotropy
SRT	0.009449	0.007382	0.004635	0.004312
MRT	0.003842	0.0006909	0.0003455	0.0003126

### 3.1. Analysis of spurious currents

The analysis of spurious currents is made by simulating a droplet in equilibrium in a domain with no gravity. Physically, the velocity of the liquid droplet and the surrounding gas should be zero, but numerically spurious currents occur at the interface of the droplet. Compared to the single relaxation time (SRT) operator, Yu et al. [34] showed that spurious currents can be reduced considerably by using the MRT collision operator. In this section, we analyze the influence of the isotropic order on our 3D MRT model. A  $64 \times 64 \times 64$  domain is used. For each simulation, a liquid droplet of initial radius  $R = 15$  lu is placed in the center of the domain. Periodic conditions were imposed in all directions. The density ratio was  $\rho_l/\rho_g \approx 40$ , which correspond to a reduced temperature  $T/T_c = 0.72$ . In the MRT model, the relaxation parameters  $s_1, s_4, s_6$  and  $s_8$  and the free parameters  $s_9, s_{11}, s_{13}, s_{17}, s_{18}$  and  $s_{19}$  are set to 1.0. The relaxation parameters  $s_2, s_3, s_5, s_7, s_9$  are set to 1.1. The initial density of the field is given by:

$$\rho(x, y, z) = \frac{\rho_{liq} + \rho_{gaz}}{2} - \frac{\rho_{liq} - \rho_{gaz}}{2} \tanh\left(\frac{2(r - R)}{W}\right) \quad (32)$$

with  $r = \sqrt{(x - x_c)^2 + (y - y_c)^2 + (z - z_c)^2}$

where  $(x_c, y_c, z_c)$  corresponds to the center of the domain.  $W$  is the initial interface width and is fixed at 3 units. The initialization of density using Eq. (32) allows a smooth transition of the density distribution and avoided numerical instability in early iterations [18]. The maximum amplitude of the spurious velocity is measured for different isotropic orders to use both the SRT and MRT operators. The results are given in Table 2.

For the same isotropy order, it can be seen that the MRT model considerably reduced the maximum amplitude of the spurious velocity compared to the SRT model. For both collision operators, the 10th order isotropy is the best choice. However, we observe that the decrease spurious velocity is not significative compared to the 8th order isotropy. Thus, the 8th order isotropy is used for the remainder of the paper.

### 3.2. Validation of Laplace's law

In the case of a three-dimensional droplet, Laplace's law is written as:

$$\Delta p = p_{in} - p_{out} = \frac{2\sigma}{R} \quad (33)$$

where  $\sigma$  is the surface tension,  $R$  is the radius of the droplet and  $p_{in}$  and  $p_{out}$  are, respectively, the pressure inside and outside the droplet. To verify Laplace's law, a series of simulations are performed by changing the radius of a static droplet as in [19]. The density ratio is  $\rho_l/\rho_g \approx 1000$  which corresponded to a reduced temperature  $T/T_c = 0.56$ . The liquid droplet of initial radius  $R_0$  is placed in the center of the domain. Periodic boundary conditions are imposed in all directions. The density is initialized using Eq. (37). When equilibrium is reached after 10 000 time-steps, the pressure difference between the inside and the outside of the droplet is measured. We assume that equilibrium is reached when  $\max |\rho^{n+1} - \rho^n| < 10^{-6}$ . Fig. 1 illustrates the convergence. The pressure differences for different values of the free parameter  $\kappa$  (Eq. (29)) with  $8 < R < 30$  are shown in Fig. 2. The markers represent the results from the numerical simulation and the solid lines represent the linear fit associated. The slope of the line gives the surface tension according to Laplace's equation. At  $\kappa = 0, 0.25, 0.5, 0.75$ , and  $0.95$ , the slopes are, respectively, equal to 0.3016, 0.2262, 0.1509, 0.0754, 0.0151 and the coefficients of determination of the linear fit are, respectively, 0.9985, 0.9971, 0.9985, 0.9996, 0.9997. The numerical results are in agreement with the linear fit. The pressure difference across the interface of the droplet is proportional to the inverse of the radius of the droplet as Laplace law's law. In addition, the results demonstrate the ability of the model to adjust the surface tension independently of density ratios and therefore without affecting the thermodynamic consistency.

### 3.3. Thermodynamic consistency

A second test to validate our model consists of verifying its thermodynamic consistency. A series of simulations on a static droplet at different temperatures  $T$  is performed as in [35]. Numerical coexistence curve is compared with the coexistence curve obtained by the Maxwell construction. A  $64 \times 64 \times 64$  domain is used. For each simulation, a static droplet of radius  $r = 15$  lu is placed at the center of the domain. Periodic boundary conditions are defined in all directions. The surface tension parameter  $\kappa$  is set to  $\kappa = 0$ . The coexistence curves are shown in Fig. 3. It is demonstrated that the results of the simulation obtained with  $A = -0.55$  are in good agreement with the coexistence curve obtained by the Maxwell construction of the liquid and vapor branches. Thus, the ability of the 3D-MRT model to simulate high density ratios while ensuring the thermodynamic consistency is confirmed.



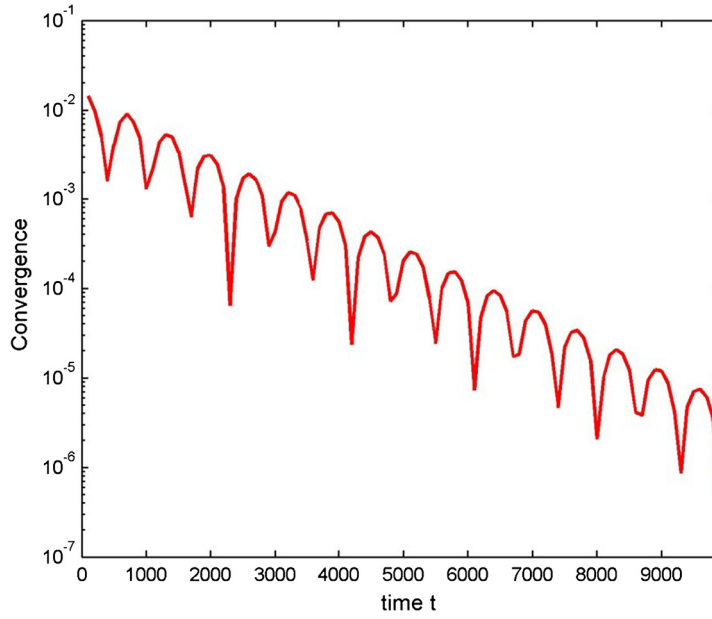


Fig. 1. Convergence.

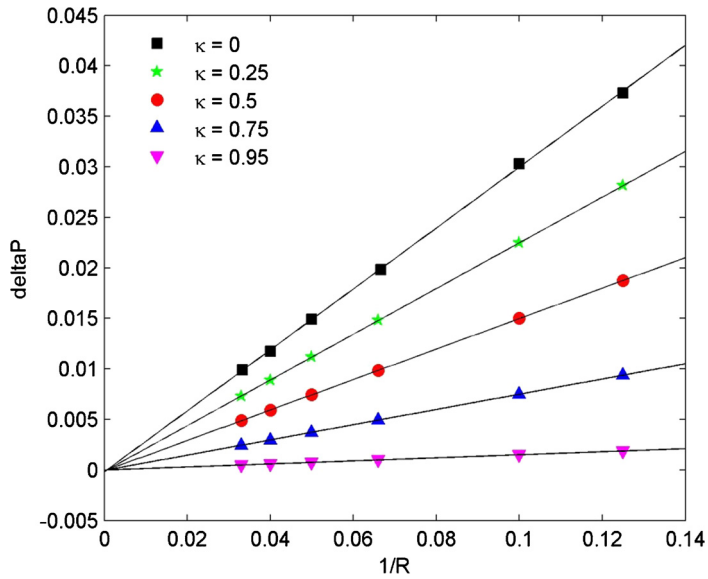


Fig. 2. Pressure difference across the interface according to the inverse of the radius.

### 3.4. Contact angle

This section presents the results of studies on the contact angle between a liquid droplet and a solid wall. By varying the parameter  $\rho_w$ , different contact angles and also different wettability surfaces, hydrophilic, neutral, or hydrophobic are obtained. For each simulation, a liquid droplet of radius  $R = 15$  lu is initialized tangent to the bottom wall. The domain size is  $64 \times 64 \times 64$ . Periodical conditions are defined on all sides of the domain and half bounce back boundary conditions were defined on the top and bottom. Fig. 4 represents the density distribution at the central plane of the domain.

When equilibrium is reached, the contact angle is measured. It is determined geometrically based on [31]. From the base  $b$ , height  $h$  and radius  $r$  of the droplet, the contact angle  $\theta$  is calculated using the expression:

$$\theta = \pi - \arctan\left(\frac{b/2}{r-h}\right) \quad (34)$$

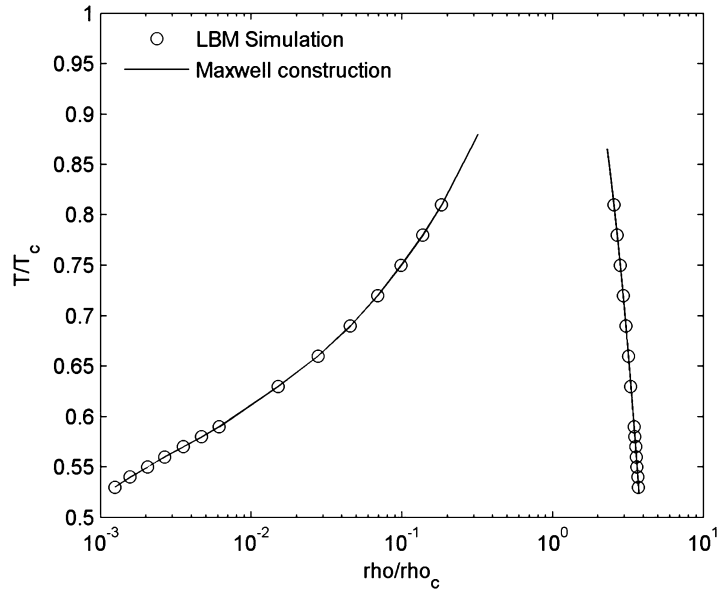


Fig. 3. Numerical coexistence curves and coexistence curves given by the Maxwell construction.

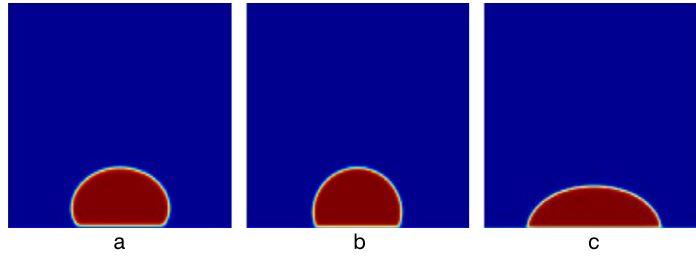


Fig. 4. (a) Hydrophobic surface; (b) neutral surface; (c) hydrophilic surface.

Where the radius  $r$  of the droplet is calculated using:

$$r = \frac{4h^2 + b^2}{8h} \quad (35)$$

The contact angles measured for the hydrophobic surface, neutral surface and hydrophilic surface are respectively  $\theta_w = 112^\circ$ ,  $\theta_w = 90^\circ$ ,  $\theta_w = 78^\circ$ . Fig. 5 shows the relationship between the contact angle  $\theta$  and the parameter  $\rho_w$ . The contact angle varies linearly with the parameter  $\rho_w$ .

### 3.5. Droplet oscillation

We then studied the dynamic problem of droplet oscillation. Initially, a deformed droplet of ellipsoid shape is placed at the center of the domain and the surface of the droplet is given by the equation:

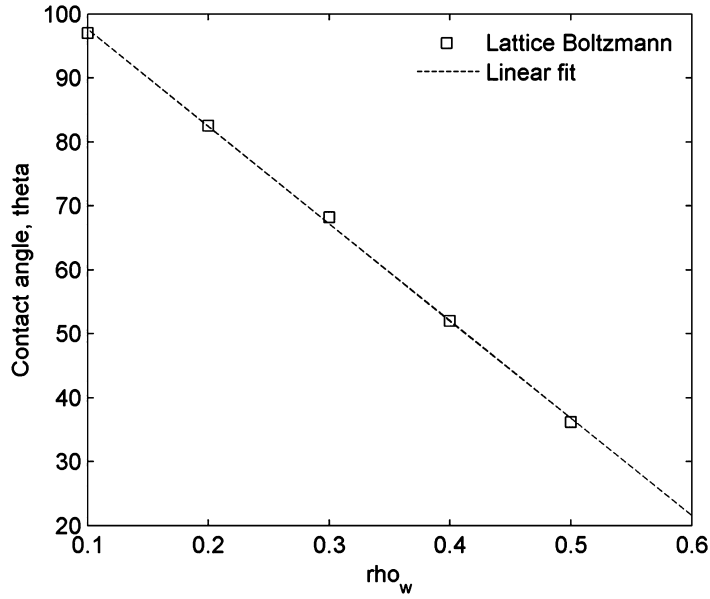
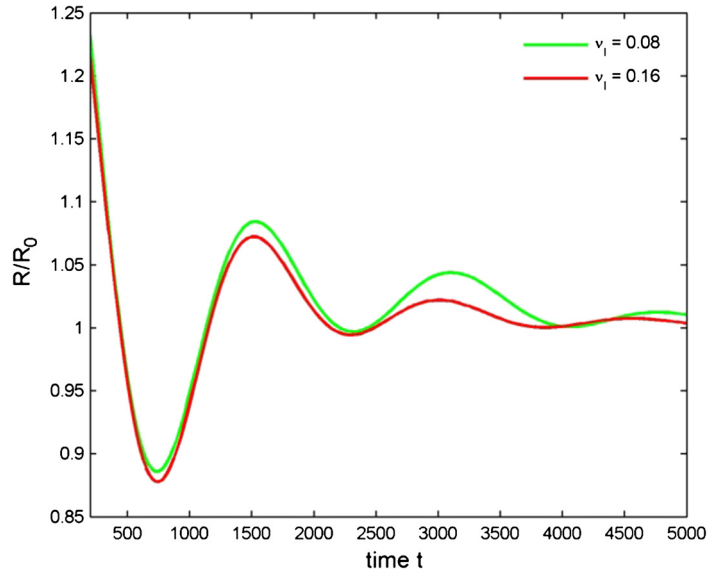
$$\frac{(x - x_c)^2}{R^2} + \frac{(y - y_c)^2}{R^2} + \frac{(z - z_c)^2}{3R^2} = 1 \quad (36)$$

where  $(x_c, y_c, z_c)$  is the center of the deformed droplet and  $R$  was its radius. The domain size is  $64 \times 64 \times 64$  and the radius  $R$  is fixed at  $R = 15$  lu. Periodic boundary conditions are imposed in all directions. Under the effect of surface tension and viscosity, the deformed droplet oscillates until it reaches a spherical shape at equilibrium. The frequency for the  $n$ th oscillation mode of a droplet is given by the analytical solution of Miller and Scriven [36]:

$$\omega_n = \omega_n^* - \frac{1}{2} \chi \omega_n^{*\frac{1}{2}} + \frac{1}{2} \chi^2 \quad (37)$$

where  $\omega_n$  is the angular response frequency and  $\omega_n^*$  is Lamb's natural resonance frequency given by [37]:

$$(\omega_n^*)^2 = \frac{n(n+1)(n-1)(n+2)}{R_d^3[n\rho_g + (n+1)\rho_l]} \sigma \quad (38)$$

Fig. 5. Contact angle in function  $\rho_w$  parameter.Fig. 6. Evolution of the normalized radius of the droplet in the horizontal direction for different viscosities  $\nu$ ,  $\kappa = 0$ .

where  $R_d$  is the equilibrium radius of the droplet and  $\sigma$  is the surface tension. The parameter  $\chi$  was given by:

$$\chi = \frac{(2n+1)^2 (\mu_l \mu_g \rho_l \rho_g)^{\frac{1}{2}}}{2^{\frac{1}{2}} R_d [n \rho_g + (n+1) \rho_l] [(\mu_l \rho_l)^{\frac{1}{2}} + (\mu_g \rho_g)^{\frac{1}{2}}]} \quad (39)$$

where  $\mu_l$  and  $\mu_g$  are, respectively, the dynamic viscosities of the liquid and the gas phases. Using the initial condition given by Eq. (36), the second oscillation mode ( $n = 2$ ) is excited. Fig. 6 illustrates the evolution of the normalized radius  $R/R_0$  of the droplet in the horizontal direction for different viscosities  $\nu$ .  $R$  is the radius of the center of the droplet at the interface in the horizontal direction and  $R_0$  is the radius of the droplet at equilibrium. Under the effect of viscous dissipation, the oscillation amplitude decreases. It is also observed that the droplet returns to its spherical shape after a longer period when the viscosity is decreased. For the second oscillation mode, we compare the analytical oscillation period  $T = 2\pi/\omega_n$  obtained by Eq. (37) and the oscillation period calculated by our model. For viscosities  $\nu = 0.08$  and  $\nu = 0.16$ , the analytical oscillation periods are  $T_a = 1639$  lu/s and  $T_a = 1702$  lu/s and the numerical oscillation periods are  $T_n = 1575$  lu/s and  $T_n = 1625$  lu/s respectively. Thus, the difference is 3.9% and 4.5% respectively. These differences are consistent with those

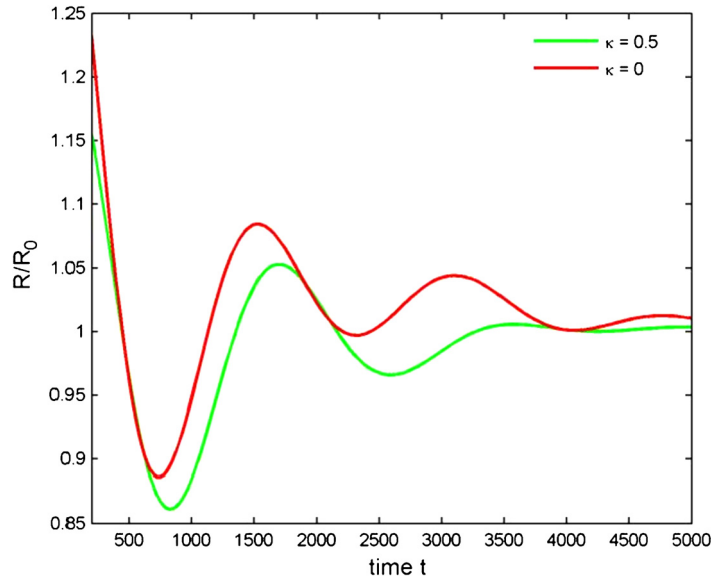


Fig. 7. Evolution of the normalized radius of the droplet in the horizontal direction for different tension surface parameters  $\kappa$ ,  $\nu = 0.16$ .

obtained in [19,23]. In addition, to validate our results, we compare the oscillation period ratios  $T^{\nu=0.16}/T^{\nu=0.08}$  in the analytical and numerical case. In the analytic and numerical case, the oscillation period ratios are 1.0384 and 1.0317. The numerical results are in good agreement with the analytical results. In a second step, we study the influence of surface tension on dynamic oscillations by varying the surface tension parameter  $\kappa$ . The viscosity is chosen to be 0.16. Fig. 7 illustrates the evolution of the radius of the droplet in the horizontal direction for different surface tension parameters  $\kappa$ . For the viscosity  $\nu = 0.16$  and the parameter  $\kappa = 0.5$ , the numerical and analytical oscillation periods are  $T_a = 1775$  lu/s and  $T_n = 1868$  lu/s respectively. The difference is less than 5%. We obtain oscillation period ratios  $T^{\kappa=0.5}/T^{\kappa=0}$  in the analytical and numerical case of 1.0429 and 1.1495 respectively. The results are acceptable. Thus, by increasing the surface tension parameter, the surface tension decreases and therefore, the oscillation period becomes longer. For a given viscosity, the influence of the viscosity increases when the surface tension is decreased.

### 3.6. Droplet impingement on a dry wall

In this section, the result of applying the new 3D-MRT model to the problem of a droplet impacting on a dry surface is presented. The domain size  $104 \times 104 \times 104$  is used. A droplet of radius  $r = 15$  lu is initially placed in the center of the domain. Periodical boundary conditions are defined on all sides of the domain and half bounce back conditions are defined on the top and bottom boundaries. The density ratio is  $\rho_l/\rho_g \approx 1000$  which correspond to a reduced temperature  $T/T_c = 0.56$ . The gravity force is imposed to simulate the fall of the droplet on the lower wall.

The study of droplet impact on a solid wall is based on three dimensionless parameters: the Reynolds number ( $Re$ ), the Weber number ( $We$ ) and the Ohnesorge ( $Oh$ ) number and are defined by:

$$Re = \frac{\rho_L D U^2}{\mu_L} \quad (40)$$

$$We = \frac{\rho_L D U^2}{\sigma} \quad (41)$$

$$Oh = \frac{\mu}{\sqrt{D \sigma \rho}} = \frac{\sqrt{We}}{Re} \quad (42)$$

where  $\rho_L$  is the liquid density,  $\mu_L$  the liquid dynamic viscosity,  $\sigma$  the surface tension, and  $D$  is the diameter of the liquid droplet. The Reynolds number  $Re$  represents the ratio of inertia force to viscous forces and the Weber number represents the droplet kinetic energy on the impact to the surface tension energy. The Ohnesorge number is a combination of Weber and Reynolds numbers.

In general, two impact regimes can occur at the impact of a droplet on a dry surface: the spreading or the splashing. Mundo et al. [38] defined the transition between the two impact regimes based on the Ohnesorge number and Reynolds number by  $K = Oh \cdot Re^{1.25}$  with  $K_{limit} = 57.7$ . For values of  $K'$  below  $K'_{limit}$ , the spreading of the droplet occurs, while for higher values, the splashing forms.

In the present paper, the simulation of the liquid droplet impacting on the dry wall is performed for  $Re = 148$  and  $We = 32.4$ . The parameter  $K$  is equal to 19.8 which is below the limit value, the spreading of the droplet on the surface is

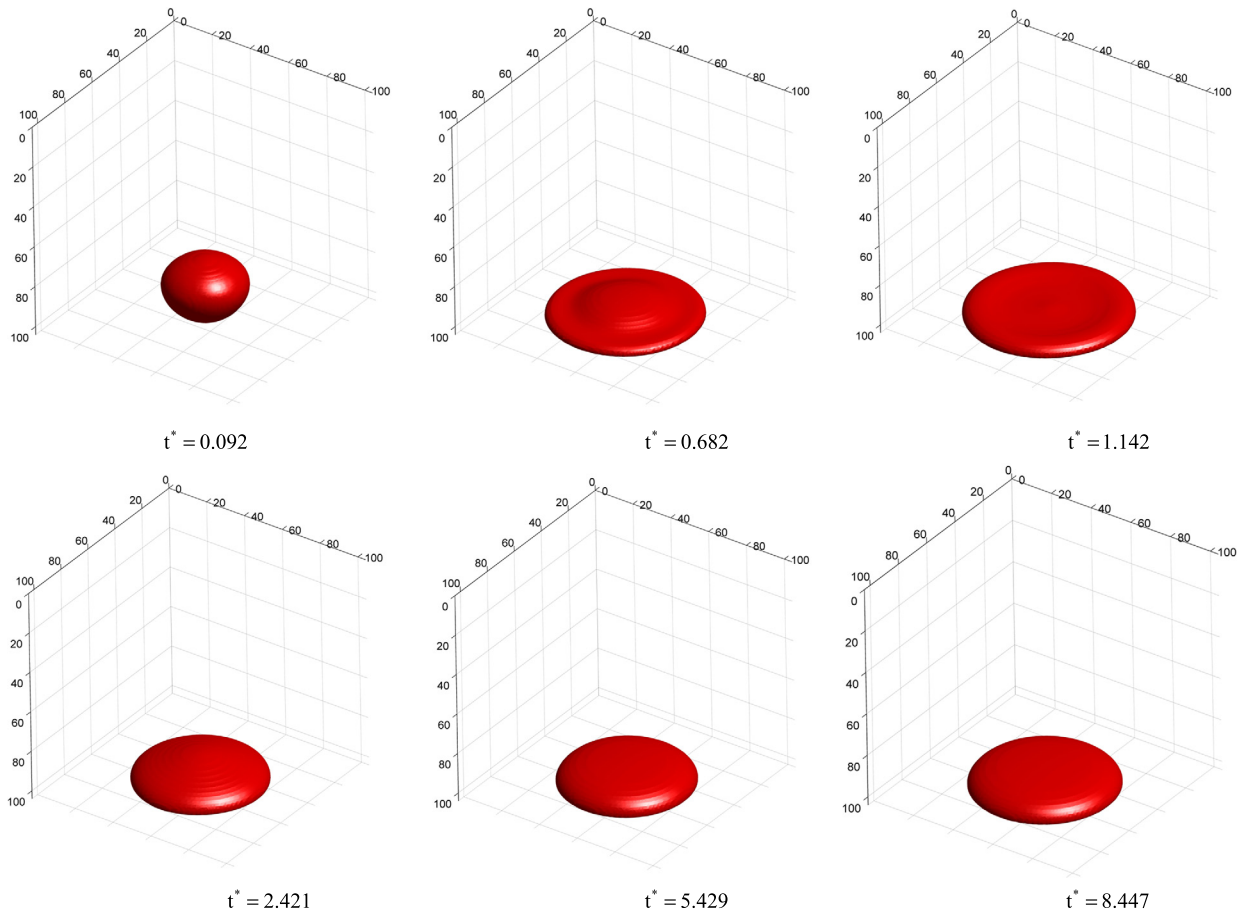


Fig. 8. Snapshots of the droplet impact process on the dry wall.

then observed as shown in Fig. 8. The snapshots showing the time evolution of the droplet shape corresponding to different dimensionless times are shown in this Fig. 8. This dimensionless time was defined by  $t^* = tU/D$  with  $U$  the impact velocity,  $D$  the droplet diameter and  $t$  the time. Shortly after the impact, at  $t^* = 0.092$ , the droplet resembles a truncated sphere. The droplet continues to fall and spread in all directions. A lamella is formed at  $t^* = 0.682$ , which reaches its maximum spreading and then retracts.

After a series of oscillations between spreading and retracting, the liquid drop reaches an equilibrium state.

The maximum spread factor defined as the ratio of the spreading film diameter on the wall to the initial droplet diameter  $D$  is calculated as a function of dimensionless time  $t^*$ . The spread factor evolution is shown in Fig. 9 for  $Re = 148$ ,  $We = 32.4$  and  $\theta_w \approx 90^\circ$ . This evolution is divided into four distinct phases: the kinematic phase, the spreading phase, the relaxation phase and the equilibrium phase [39]. The kinematic phase corresponds to the first-time interval during the impingement of the droplet on the wall. It is conducted up to a dimensionless time  $t^* = 0.1$ . During this phase, the inertia force predominates and the liquid droplet resembles a truncated sphere. Fig. 10 represents the spread factor evolution during the kinematic phase of four different cases with varying  $Re$  and  $We$  number. This Fig. 10 shows that, in the kinematic phase, the spread factor is independent of the physical properties  $Re$  and  $We$  but depends only on the dimensionless time  $t^*$ . A curve fit  $D^* = 2.2t^{0.5}$  of our numerical spread factor is also shown in this Fig. 10. Rioboo et al. [39] showed that the spread factor is proportional to  $t^{0.5}$  with a coefficient of 2.8 determined from experimental data. The results obtained from our LBM model are in agreement with the experimental results of Rioboo et al. [39].

Contrary to the kinematic phase, the maximum spread factor depends on the  $Re$  and  $We$  number. Fig. 11 shows the comparison between the maximum spread factor obtained from our LBM model and results from the literature [40–42]. The numerical results are well in agreement.

The influence of the parameter  $\kappa$  on the dynamic impact of a droplet on a dry surface is analyzed by maintaining the Reynolds number and the contact angle at 148 and  $92^\circ$  respectively. Increasing the  $\kappa$  value decreases the surface tension and thus increases the Weber number. Using values of  $\kappa$  equal to 0, 0.5, 0.95, we obtain respectively Weber number of 32, 48 and 61. The Fig. 12 shows that the evolution of the impact process of the droplet is similar to the different values of  $\kappa$ . A maximum spread factor of 1.85, 1.89 and 1.92 was obtained respectively for  $\kappa$  equal to 0, 0.5, 0.95. Thus, the influence of  $\kappa$  and therefore the Weber number on the maximum spread factor is relatively weak. This result is consistent with the

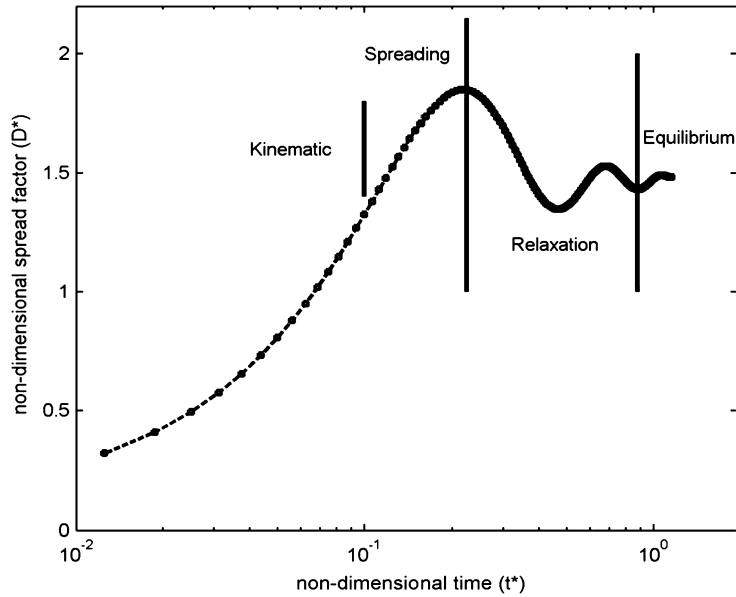


Fig. 9. Time evolution of the spread factor.

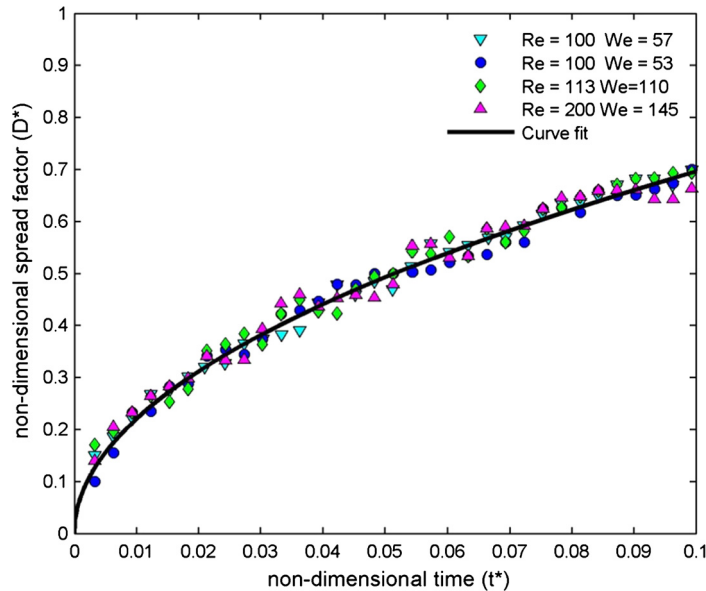


Fig. 10. Spread factor during kinematic phase at different  $Re$  and  $We$ .

study of Ref. [39]. In general, the increase in  $\kappa$  shows no significant increase of the spread factor in the case of the spread of the droplet on the wall. The reason is that the viscous force plays a major role in the flow. However, a significant decrease in the surface tension may change the impact regime and leads to the splashing of the droplet.

Finally, we analyze the effect of surface wettability on the spread factor. Fig. 13 illustrates the spread factor time evolution for different surface wettability. Three types of surfaces are studied: hydrophilic, neutral, hydrophobic, with contact angles  $\theta_w = 61^\circ$ ,  $\theta_w = 90^\circ$ ,  $\theta_w = 103^\circ$  respectively. The three curves representing the spread factor are similar during the kinematics phase (before  $t^* = 0.1$ ), indicating that the wettability has a weak effect during this phase. However, during the spreading phase (after  $t^* = 0.1$ ), differences are more important, particularly in the maximum spread factor. With a hydrophilic surface, the largest spread factor is achieved with a maximum of 2.3. For the hydrophobic surface, the spread factor is the lowest with a maximum of 1.5. In addition, more intense oscillations are observed during the relaxation phase for a hydrophobic surface and the equilibrium is reached later. On the other hand, for a hydrophilic surface, equilibrium is achieved rapidly with little oscillations. In conclusion, the surface wettability influences the spread factor and also the time required to reach equilibrium.

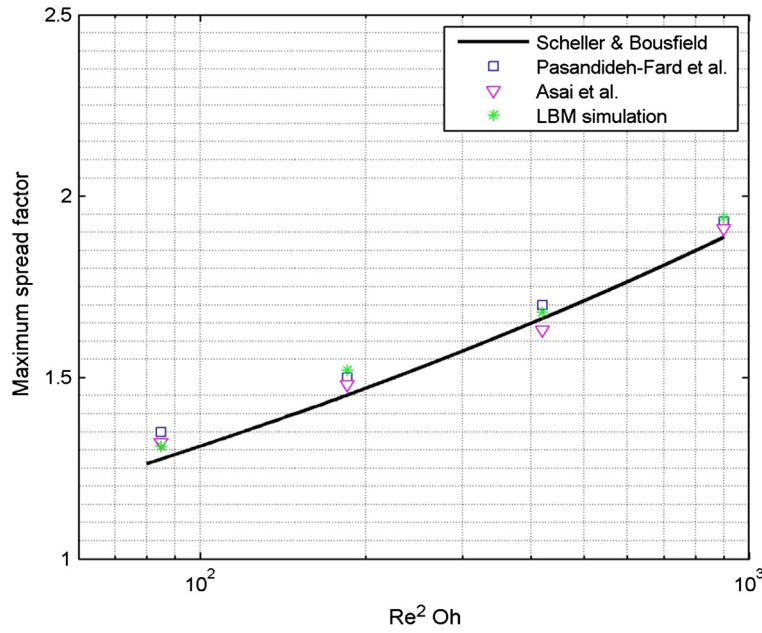


Fig. 11. Comparison of maximum spread factor between our numerical results and prediction equation.

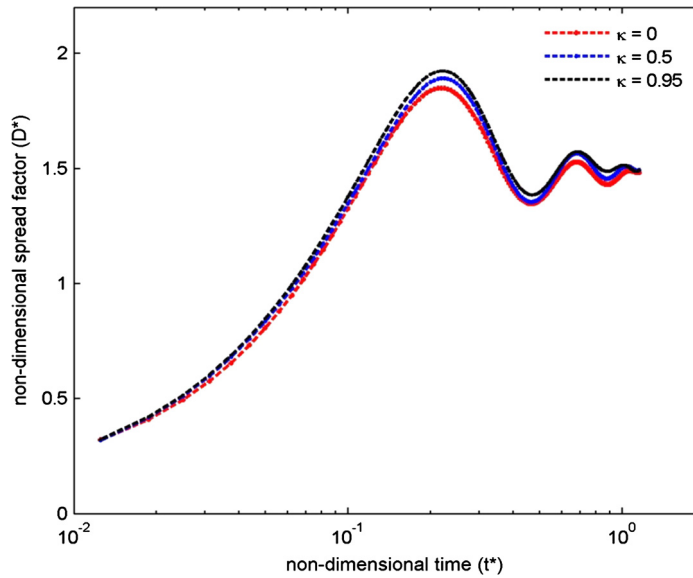


Fig. 12. Evolution of the spread factor for different  $\kappa$  values.

### 3.7. Droplet impact on a wet surface

The problem of liquid droplet impacting a wet surface is encountered in many engineering applications, such as the ink-jet printer, or the spray injection in internal combustion engines [43,44]. For the impact of a droplet on a wet surface, the Reynolds number  $Re$ , Weber number  $We$ , Ohnesorge number  $Oh$  are also important physical parameters.

Experimental tests [45,46] have shown that two situations may arise in this problem: the droplet spreading in the liquid film or the splash of the droplet. The transition between the spreading and the splashing of the droplet depends on the normal speed, the diameter of the droplet, the surface tension, and the viscosity. Overall, studies [47,48] show that a small liquid film thickness promotes the splashing while a thick liquid film delays its appearance and enhances the coalescence of the droplet with the liquid fluid layer. Several correlations [47–49] are present in the literature to determine the transition, but the most complete study is the work of Cossali et al. [49] who propose a correlation depending on the dimensionless thickness of the liquid film  $\delta = h/D$ , where  $h$  is the thickness of the liquid layer and  $D$  the diameter of the droplet. This correlation is given by  $K' = We \cdot Oh^{-0.4}$  with  $K'_{limit} = 2100 + 5880 \cdot \delta^{1.44}$ . For values of  $K'$  below  $K'_{limit}$  the spreading of the

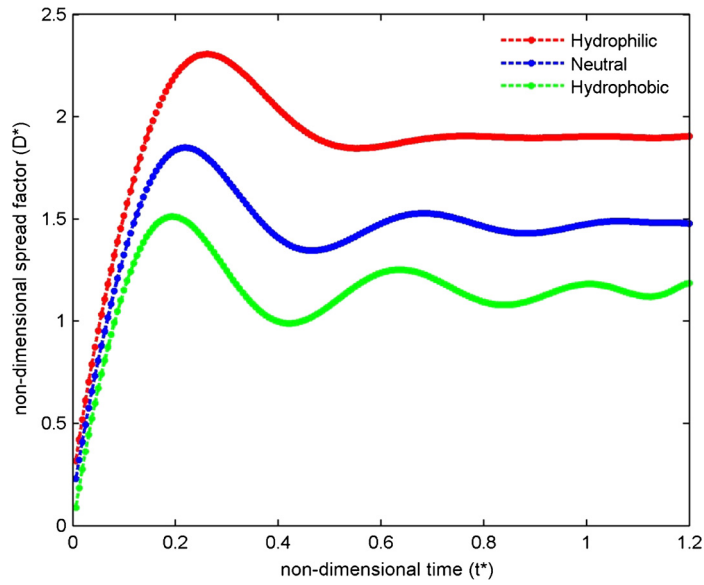


Fig. 13. Influence of wettability on the spread factor.

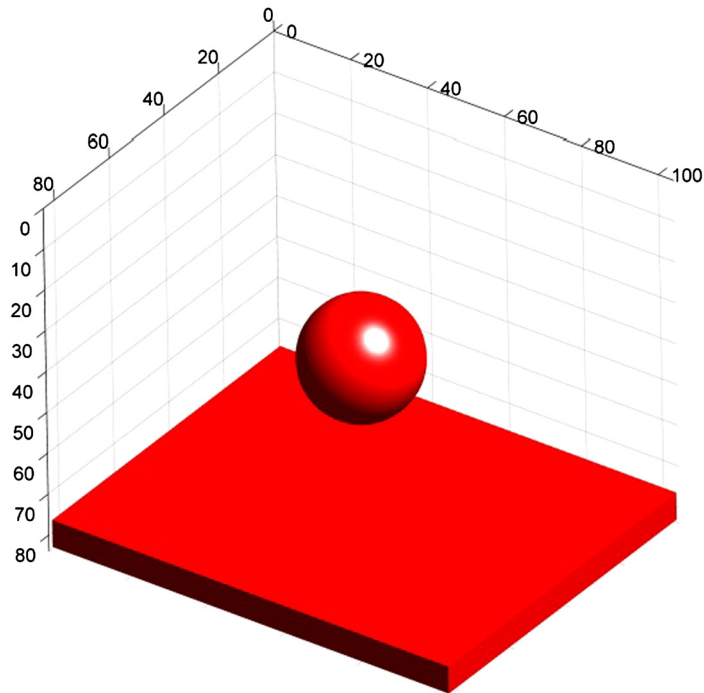


Fig. 14. Simulation of the initial step.

droplet occurs, while for higher values, the splashing forms. In addition, studies of Rioboo et al. [45] show that for values of  $K'$  between 100 and 1000, the spread of the droplet spread is observed.

In the present test case, the Reynolds number and the Weber number are set at 120 and 33 respectively. The dimensionless thickness  $\delta$  is set to 0.53, giving a value  $K' = 111$  which is less than  $K'_{limit} = 4478$ . Initially, a liquid droplet of radius  $r = 15$  lu was placed in the center of the domain, as illustrated in Fig. 14.

The 3D-MRT model is applied, and an  $84 \times 84 \times 104$  domain is used. The density ratio is  $\rho_l/\rho_g \approx 1000$  which corresponded to a reduced temperature  $T/T_c = 0.56$ . The gravity force is imposed. Periodical boundary conditions are defined on all sides of the domain and half bounce back conditions are defined on the top and bottom boundaries. The impact process of a droplet on a film liquid is shown in Fig. 15. We observe the spreading droplet on the liquid film and the transverse



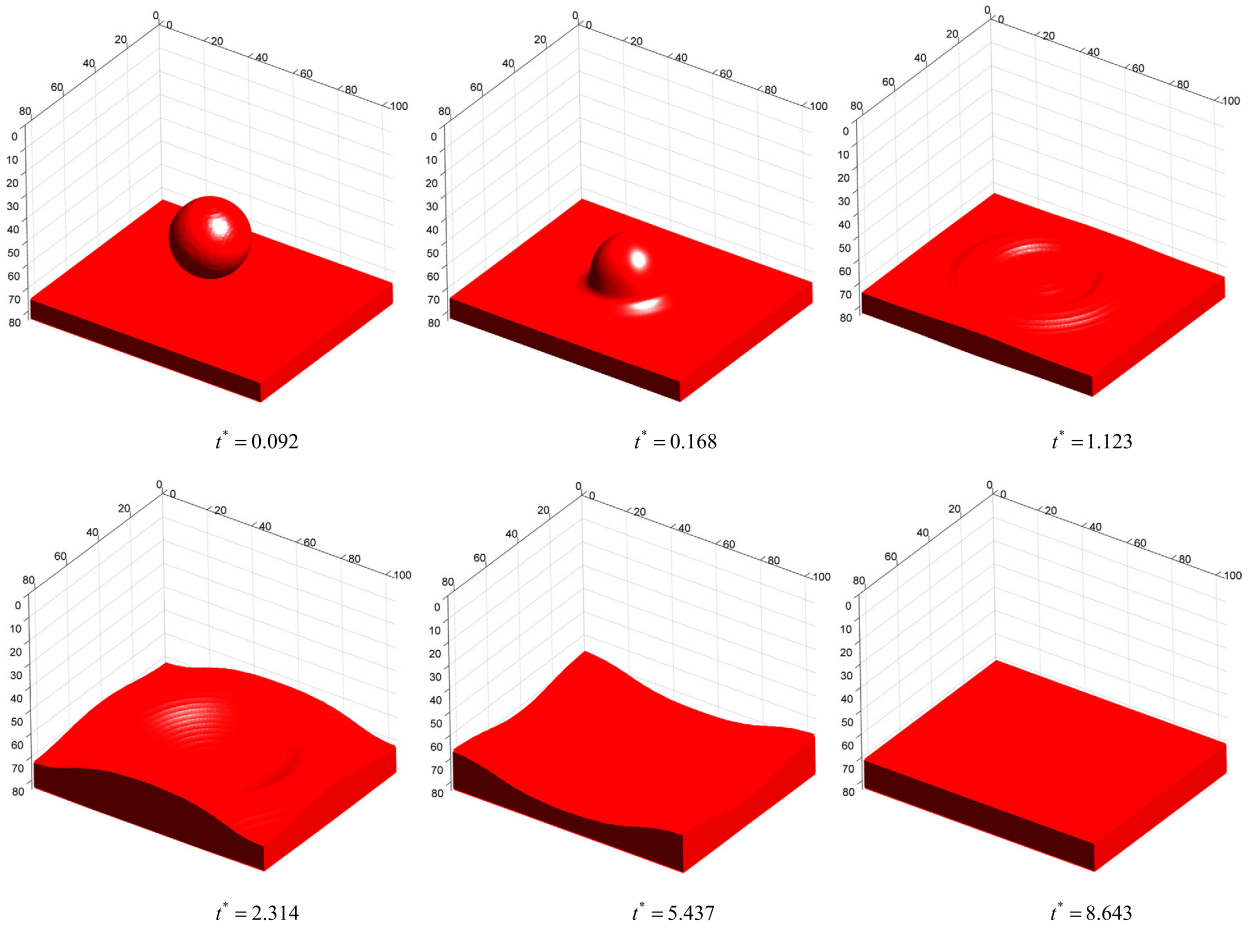


**Fig. 15.** Snapshots of the droplet impact process on the wet surface.

wave's propagation on the surface. The transverse waves propagate in the radial direction. After a considerable time, the droplet disappears and the final solution is a stationary fluid (Fig. 15).

The influence of  $\kappa$  on the dynamic impact of a droplet on a wet surface is studied by measuring the dimensionless fluid height moved  $e = h_{max}/D$ .  $h_{max}$  is the maximum height of the liquid film moved and  $D$  the diameter of the droplet. The Reynolds number is set to 120. For  $\kappa$  values equal to 0, 0.5 and 0.95, the dimensionless height  $e$  obtained is respectively 1.4, 1.47 and 1.47. Between  $\kappa = 0$  and  $\kappa = 0.5$ , the increase of the maximum height of the liquid film is only 5%, but remains similar to the values of  $\kappa = 0.5$  and  $\kappa = 0.95$ . The influence of  $\kappa$  on the maximum height of the fluid moved is relatively low. Capillary effects predominate on the inertia of the droplet and oppose fluid movement. However, as demonstrated by Ramirez et al. [50], the surface tension may play an important role in the case of the impact of a droplet with a splash. It has shown that the reduction in surface tension would lead to the increase of secondary droplets and a decrease in their diameter.

#### 4. Conclusion

In the present study, we propose a new 3D-MRT multiphase LBM model with variable surface tension. An analysis of the spurious velocity for different isotropic order is made and showed the influence of isotropy orders when the MRT operator is used. It is demonstrated that an order of isotropy of 8 is sufficient to achieve acceptable accuracy. The 3D-MRT model is validated through Laplace's law and is able to simulate a high density ratio between two phases while maintaining thermodynamic consistency. In addition, the surface tension is adjustable without change to the density ratio. The oscillation dynamics of a deformed droplet are studied, and the numerical results are in agreement with the analytical solution. The relationship between the contact angle  $\theta_w$  and the parameter  $\rho_w$  is found to follow a linear trend. The model is used to simulate the droplet impact on a dry surface and is able to represent the four phases of the droplet impact process: kinematic, spreading, relaxation and equilibrium. It is shown that the kinematic phase is only a function of dimensionless time and not physical properties. The results of the simulation are in agreement with the experimental data of Rioboo et al. [39]. In addition, the influence of surface wettability on the maximum spread factor is identified. A hydrophilic surface led

to a higher spread factor and equilibrium is reached more quickly. For a hydrophobic surface, the time to reach equilibrium is longer. Finally, the model is applied to the simulation of the droplet impact on a wetted surface and we observe the transverse wave's propagation on the surface.

## Acknowledgements

This work was supported by Natural Sciences and Engineering Research Council of Canada (NSERC), under grant number RGPIN-2016-06427.

## References

- [1] D. Gueyffier, J. Li, A. Nadim, R. Scardovelli, S. Zaleski, Volume-of-fluid interface tracking with smoothed surface stress methods for three-dimensional flows, *J. Comput. Phys.* 152 (1999) 423–456.
- [2] C.W. Hirt, B.D. Nichols, Volume of fluid (VOF) method for the dynamics of free boundaries, *J. Comput. Phys.* 39 (1981) 201–225.
- [3] W.J. Rider, D.B. Kothe, Reconstructing volume tracking, *J. Comput. Phys.* 141 (1998) 112–152.
- [4] S. Osher, Level set methods, in: *Geometric Level Set Methods in Imaging, Vision, and Graphics*, Springer, 2003, pp. 3–20.
- [5] J. Sethian, P. Smereka, Level set methods for fluid interfaces, *Annu. Rev. Fluid Mech.* 35 (2003) 341–372.
- [6] S. Chen, G.D. Doolen, Lattice Boltzmann method for fluid flows, *Annu. Rev. Fluid Mech.* 30 (1998) 329–364.
- [7] S. Leclaire, Étude d'un modèle de Boltzmann sur réseau pour la simulation assistée par ordinateur des fluides à plusieurs phases immiscibles, *École Polytechnique de Montréal*, 2013.
- [8] D.H. Rothman, J.M. Keller, Immiscible cellular-automaton fluids, *J. Stat. Phys.* 52 (1988) 1119–1127.
- [9] X. Shan, H. Chen, Lattice Boltzmann model for simulating flows with multiple phases and components, *Phys. Rev. E* 47 (1993) 1815.
- [10] M.R. Swift, E. Orlandini, W. Osborn, J. Yeomans, Lattice Boltzmann simulations of liquid–gas and binary fluid systems, *Phys. Rev. E* 54 (1996) 5041.
- [11] M.R. Swift, W. Osborn, J. Yeomans, Lattice Boltzmann simulation of nonideal fluids, *Phys. Rev. Lett.* 75 (1995) 830.
- [12] X. Shan, G. Doolen, Multicomponent lattice-Boltzmann model with interparticle interaction, *J. Stat. Phys.* 81 (1995) 379–393.
- [13] L. Chen, Q. Kang, Y. Mu, Y.-L. He, W.-Q. Tao, A critical review of the pseudopotential multiphase lattice Boltzmann model: methods and applications, *Int. J. Heat Mass Transf.* 76 (2014) 210–236.
- [14] A. Kupershtokh, D. Medvedev, D. Karpov, On equations of state in a lattice Boltzmann method, *Comput. Math. Appl.* 58 (2009) 965–974.
- [15] P. Yuan, L. Schaefer, Equations of state in a lattice Boltzmann model, *Phys. Fluids* (1994–present) (18) (2006) 042101.
- [16] M. Sbragaglia, R. Benzi, L. Biferale, S. Succi, K. Sugiyama, F. Toschi, Generalized lattice Boltzmann method with multirange pseudopotential, *Phys. Rev. E* 75 (2007) 026702.
- [17] X. Shan, Analysis and reduction of the spurious current in a class of multiphase lattice Boltzmann models, *Phys. Rev. E* 73 (2006) 047701.
- [18] H. Huang, M. Krafczyk, X. Lu, Forcing term in single-phase and Shan–Chen-type multiphase lattice Boltzmann models, *Phys. Rev. E* 84 (2011) 046710.
- [19] Q. Li, K. Luo, Achieving tunable surface tension in the pseudopotential lattice Boltzmann modeling of multiphase flows, *Phys. Rev. E* 88 (2013) 053307.
- [20] A. Xu, T. Zhao, L. An, L. Shi, A three-dimensional pseudo-potential-based lattice Boltzmann model for multiphase flows with large density ratio and variable surface tension, *Int. J. Heat Fluid Flow* 56 (2015) 261–271.
- [21] A.L. Kupershtokh, Criterion of numerical instability of liquid state in LBE simulations, *Comput. Math. Appl.* 59 (2010) 2236–2245.
- [22] A.L. Kupershtokh, A lattice Boltzmann equation method for real fluids with the equation of state known in tabular form only in regions of liquid and vapor phases, *Comput. Math. Appl.* 61 (2011) 3537–3548.
- [23] A. Hu, L. Li, R. Uddin, Surface tension adjustment in a pseudo-potential lattice Boltzmann model, *arXiv:1412.7228*, 2014.
- [24] Z. Guo, C. Zheng, B. Shi, Discrete lattice effects on the forcing term in the lattice Boltzmann method, *Phys. Rev. E* 65 (2002) 046308.
- [25] Y. Qian, D. d'Humières, P. Lallemand, Lattice BGK models for Navier–Stokes equation, *Europhys. Lett.* 17 (1992) 479.
- [26] D. d'Humières, Multiple-relaxation-time lattice Boltzmann models in three dimensions, *Philos. Trans. R. Soc., Math. Phys. Eng. Sci.* 360 (2002) 437–451.
- [27] S. Mukherjee, J. Abraham, A pressure-evolution-based multi-relaxation-time high-density-ratio two-phase lattice-Boltzmann model, *Comput. Fluids* 36 (2007) 1149–1158.
- [28] K.N. Premnath, J. Abraham, Three-dimensional multi-relaxation time (MRT) lattice-Boltzmann models for multiphase flow, *J. Comput. Phys.* 224 (2007) 539–559.
- [29] N.S. Martys, H. Chen, Simulation of multicomponent fluids in complex three-dimensional geometries by the lattice Boltzmann method, *Phys. Rev. E* 53 (1996) 743.
- [30] H. Huang, D.T. Thorne Jr, M.G. Schaap, M.C. Sukop, Proposed approximation for contact angles in Shan-and-Chen-type multicomponent multiphase lattice Boltzmann models, *Phys. Rev. E* 76 (2007) 066701.
- [31] S. Schmieschek, J. Harting, Contact angle determination in multicomponent lattice Boltzmann simulations, *arXiv:0910.3915*, 2009.
- [32] X. Xing, D.L. Butler, C. Yang, A lattice Boltzmann based single-phase method for modeling surface tension and wetting, *Comput. Mater. Sci.* 39 (2007) 282–290.
- [33] Y. Yan, Y. Zu, A lattice Boltzmann method for incompressible two-phase flows on partial wetting surface with large density ratio, *J. Comput. Phys.* 227 (2007) 763–775.
- [34] Z. Yu, L.-S. Fan, Multirelaxation-time interaction-potential-based lattice Boltzmann model for two-phase flow, *Phys. Rev. E* 82 (2010) 046708.
- [35] B. Wen, Z. Qin, C. Zhang, H. Fang, Thermodynamic-consistent lattice Boltzmann model for nonideal fluids, *Europhys. Lett.* 112 (2015) 44002.
- [36] C. Miller, L. Scriven, The oscillations of a fluid droplet immersed in another fluid, *J. Fluid Mech.* 32 (1968) 417–435.
- [37] H. Lamb, *Hydrodynamics*, Cambridge University Press, 1932.
- [38] C. Mundo, M. Sommerfeld, C. Tropea, Experimental studies of the deposition and splashing of small liquid droplets impinging on a flat surface, in: *Proceedings of ICLASS-94*, 1994, pp. 134–141.
- [39] R. Rioboo, M. Marengo, C. Tropea, Time evolution of liquid drop impact onto solid, dry surfaces, *Exp. Fluids* 33 (2002) 112–124.
- [40] A. Asai, M. Shiota, S. Hirasawa, T. Okazaki, Impact of an ink drop on paper, *J. Imaging Sci. Technol.* 37 (1993) 205–207.
- [41] M. Pasandideh-Fard, Y. Qiao, S. Chandra, J. Mostaghimi, Capillary effects during droplet impact on a solid surface, *Phys. Fluids* (1994–present) (8) (1996) 650–659.
- [42] B.L. Scheller, D.W. Bousfield, Newtonian drop impact with a solid surface, *AIChE J.* 41 (1995) 1357–1367.
- [43] M.L. Sadley, D.A. Dean, Fuel injection system employing solid-state injectors for liquid fueled combustion engines, *Google Patents*, 1995.
- [44] M. Showalter, *Injection spray systems*, Google Patents, 1973.
- [45] R. Rioboo, C. Bauthier, J. Conti, M. Voue, J. De Coninck, Experimental investigation of splash and crown formation during single drop impact on wetted surfaces, *Exp. Fluids* 35 (2003) 648–652.
- [46] D.A. Weiss, A.L. Yarin, Single drop impact onto liquid films: neck distortion, jetting, tiny bubble entrainment, and crown formation, *J. Fluid Mech.* 385 (1999) 229–254.

- [47] I. Roisman, L. Araneo, M. Marengo, C. Tropea, Evaluation of drop impingement models: experimental and numerical analysis of a spray impact, in: Thirteenth Annual Conference on Liquid Atomization and Spray Systems ILASS-Europe, Florence, Italy, 1999.
- [48] W. Samenfink, A. Elsässer, K. Dullenkopf, S. Wittig, Droplet interaction with shear-driven liquid films: analysis of deposition and secondary droplet characteristics, *Int. J. Heat Fluid Flow* 20 (1999) 462–469.
- [49] G. Cossali, A. Coghe, M. Marengo, The impact of a single drop on a wetted solid surface, *Exp. Fluids* 22 (1997) 463–472.
- [50] M. Ramirez de Santiago, Etude de l'entraînement de gouttelettes à la surface libre du liquide dans une colonne à bulles, Grenoble 1, 1991.